International Journal of Heat and Mass Transfer 52 (2009) 2471–2483

Contents lists available at ScienceDirect

International Journal of Heat and Mass Transfer

journal homepage: www.elsevier.com/locate/ijhmt

Heat flow analysis for natural convection within trapezoidal enclosures based on heatline concept

Tanmay Basak [a], S. Roy [b], I. Pop [c,*]

[a] Department of Chemical Engineering, Indian Institute of Technology Madras, Chennai 600036, India
[b] Department of Mathematics, Indian Institute of Technology Madras, Chennai 600036, India
[c] Faculty of Mathematics, University of Cluj, R-3400 Cluj, CP 253, Romania

ARTICLE INFO

Article history:
Received 15 October 2008
Available online 4 March 2009

Keywords:
Heatlines
Heatfunctions
Streamlines
Streamfunctions
Natural convection
Trapezoidal cavities
Uniform and non-uniform heating

ABSTRACT

Heat flow patterns in the presence of natural convection within trapezoidal enclosures have been analyzed with heatlines concept. In the present study, natural convection within a trapezoidal enclosure for uniformly and non-uniformly heated bottom wall, insulated top wall and isothermal side walls with inclination angle φ have been investigated. Momentum and energy transfer are characterized by streamfunctions and heatfunctions, respectively, such that streamfunctions and heatfunctions satisfy the dimensionless forms of momentum and energy balance equations, respectively. Finite element method has been used to solve the velocity and thermal fields and the method has also been found robust to obtain the streamfunction and heatfunction accurately. The unique solution of heatfunctions for situations in differential heating is a strong function of Dirichlet boundary condition which has been obtained from average Nusselt numbers for hot or cold regimes. Parametric study for the wide range of Rayleigh number $(Ra), 10^3 \leqslant Ra \leqslant 10^5$ and Prandtl number $(Pr), 0.026 \leqslant Pr \leqslant 1000$ with various tilt angles $\varphi = 45^\circ, 30^\circ$ and 0°(square) have been carried out. Heatlines are found to be continuous lines connecting the cold and hot walls and the lines are perpendicular to the isothermal wall for the conduction dominant heat transfer. The enhanced thermal mixing near the core for larger *Ra* is explained with dense heatlines and convective loop of heatlines. The formation of boundary layer on the walls has a direct consequence based on heatlines. The local Nusselt numbers have also been shown for side and bottom walls and variation of local Nusselt numbers with distance have also been explained based on heatlines. It is found that average heat transfer rate does not vary significantly with φ for non-uniform heating of bottom wall.

1. Introduction

Natural convection in enclosed cavities has received significant attention due to many engineering applications [1–5]. The extensive studies for rectangular and square enclosures using various numerical simulations reported by Patterson and Imberger [6], Nicolette et al. [7], Hall et al. [8], Hyun and Lee [9], Fusegi et al. [10], Lage and Bejan [11,12], Xia and Murthy [13] and Al-Amiri et al.[14] ensure that several attempts have been made to acquire a basic understanding of natural convection flows and heat transfer characteristics in an enclosure.

The majority of works dealing with convection in enclosures is restricted to the cases of simple geometry e.g., rectangular, square, cylindrical and spherical cavities. But the configurations of actual containers occurring in practice is often far from being simple. A few studies on natural convection on triangular enclosures filled with a viscous fluid or a porous medium have been carried out by earlier researchers [15–17]. Iyican and Bayazitoglu [18] investigated natural convective flow and heat transfer within a trapezoidal enclosure with parallel cylindrical top and bottom walls at different temperatures and plane adiabatic side walls. A critical Rayleigh number is presented depending on the tilting angle, where unicellular convection is observed. Karyakin [19] reported two-dimensional laminar natural convection in enclosures of arbitrary cross-section. This study reported on transient natural convection in an isosceles trapezoidal cavity inclined at angle ϕ to the vertical line where a single circulation region is found in the steady state case. The heat transfer rate is found to increase with the increase in angle ϕ.

Perić [20] studied natural convection in trapezoidal cavities with a series of systematically refined grids from 10×10 to 160×160 control volume and observed the convergence of results for grid independent solutions. Kuyper and Hoogendoorn [21] investigated laminar natural convection flow in trapezoidal enclosures to study the influence of the inclination angle on the flow and also the dependence of the average Nusselt number on the Ray-

* Corresponding author.
E-mail addresses: tanmay@iitm.ac.in (T. Basak), sjroy@iitm.ac.in (S. Roy), pop.ioan@yahoo.co.uk (I. Pop).

0017-9310/$ - see front matter © 2009 Elsevier Ltd. All rights reserved.
doi:10.1016/j.ijheatmasstransfer.2009.01.020

Nomenclature

g	acceleration due to gravity, ms^{-2}
k	thermal conductivity, Wm^{-1} K^{-1}
L	height or base of the trapezoidal cavity, m
N	total number of nodes
Nu	Nusselt number
p	pressure, Pa
P	dimensionless pressure
Pr	Prandtl number
R	Residual of weak form
Ra	Rayleigh number
T	temperature, K
T_h	temperature of hot bottom wall, K
T_c	temperature of cold vertical wall, K
u	x component of velocity, ms^{-1}
U	x component of dimensionless velocity
v	y component of velocity, ms^{-1}
V	y component of dimensionless velocity
X	dimensionless distance along x coordinate
x	distance along x coordinate, m
Y	dimensionless distance along y coordinate
y	distance along y coordinate, m

Greek symbols

α	thermal diffusivity, m^2 s^{-1}
β	volume expansion coefficient, K^{-1}
γ	penalty parameter
θ	dimensionless temperature
ν	kinematic viscosity, m^2 s^{-1}
ρ	density, kgm^{-3}
Φ	basis functions
ψ	streamfunction
Π	heatfunction

Subscripts

b	bottom wall
l	left wall
r	right wall
s	side wall

leigh number. Thermosolutal heat transfer within trapezoidal cavity heated at the bottom wall and cooled at the inclined top wall was investigated by Boussaid et al. [22]. Recently, studies on natural convection have been carried out for various inclinations of trapezoidal enclosures filled with either fluid or porous medium[23,24]. However, the detailed understanding of heat flows and distribution of heat energy for natural convection process in trapezoidal cavities have not been studied.

The heatlines are introduced for visualization and analysis of heat transfer [25,26]. Convective heat transfer processes were analyzed mainly using isotherms before introduction of the concept of 'heatlines'. The heatline is the best way to visualize the heat transfer in two-dimensional convective transport processes. Energy flow within various regimes especially for convective heat transport processes can be best visualized by heatlines whereas isotherms are unable to give guideline for energy flows. The heatlines are mathematically represented by heatfunctions and the proper dimensionless forms of heatfunctions are closely related to overall Nusselt numbers. Kimura and Bejan [25] proposed heatlines for visualization of convective heat transfer through an extension of heat flux line concept to include the advection terms. Further, Bejan [26] reviewed extensively various aspects of heatlines and illustrated the use of heatline concept to visualize various physical situations.

Costa [27–30] gave a unified viewpoint in both physical and numerical aspects on the treatment of heatlines for visualizing two-dimensional transport problems. Heatlines analysis have been carried out for investigations in polar coordinates [31–35]. There are few studies on the application of heatlines for natural convection by earlier workers (Bello-Ochende [36], Aggarwal and Manhapra [37], Deng and Tang [38], Zhao et al. [39]). Application of heatlines was shown for thermomagnetic convection in electroconductive melts [40,41]. A few recent investigations based on heatline approach involves convection in porous cavity [42], conjugate natural convection [43] and convection due to localized heating and salting [44]. A recent investigation is also based on applications of heatlines to analyze natural convection within porous non-isothermal triangular cavities [45]. However, visualization of heat flows via heatlines were not reported for trapezoidal enclosures. It is also essential to study the heat transfer characteristics in complex geometries in order to obtain the optimal design of the container for various industrial applications. Thus, it is important to study the energy flow using heatlines within trapezoidal enclosures.

The aim of this article is to analyze energy flows due to natural convection within trapezoidal enclosures with hot bottom wall and cold side walls in presence of insulated top walls. The main objective to study this fundamental problem is to examine thermal mixing near the central core of the cavity for various material processing applications. Numerical simulations were performed using Galerkin finite element method with penalty parameter to solve the nonlinear coupled partial differential equations for flow and temperature fields. The Galerkin method is further employed to solve the Poisson equation for streamfunctions and heatfunctions. It may be noted that Galerkin finite element method has been used here for the first time to evaluate the heatfunction. The heatline concept primarily based on the imposition of boundary conditions have been addressed first time in the present work. The heatlines and thermal mixing will be illustrated for commonly used fluid with $Pr = 0.026 - 1000$ in various industrial applications.

2. Mathematical formulation

2.1. Velocity and temperature distributions

Let us consider a trapezoidal cavity of height L with the left wall inclined at an angle $\varphi = 45^\circ, 30^\circ, 0^\circ$ with Y axis (Fig. 1a–c). The boundary conditions for velocity are considered as no-slip on solid boundaries. The fluid is considered as incompressible, Newtonian and the flow is assumed to be laminar. For the treatment of the buoyancy term in the momentum equation, Boussinesq approximation is employed to account for the variations of density as a function of temperature, and to couple in this way the temperature field to the flow field. Under these assumptions, governing equations for steady two-dimensional natural convection flow in the square cavity using conservation of mass, momentum and energy can be written with following dimensionless variables or numbers

$$X = \frac{x}{L}, \quad Y = \frac{y}{L}, \quad U = \frac{uL}{\alpha}, \quad V = \frac{vL}{\alpha}, \quad \theta = \frac{T - T_c}{T_h - T_c}$$
$$P = \frac{pL^2}{\rho\alpha^2}, \quad Pr = \frac{\nu}{\alpha}, \quad Ra = \frac{g\beta(T_h - T_c)L^3 Pr}{\nu^2} \tag{1}$$

as:

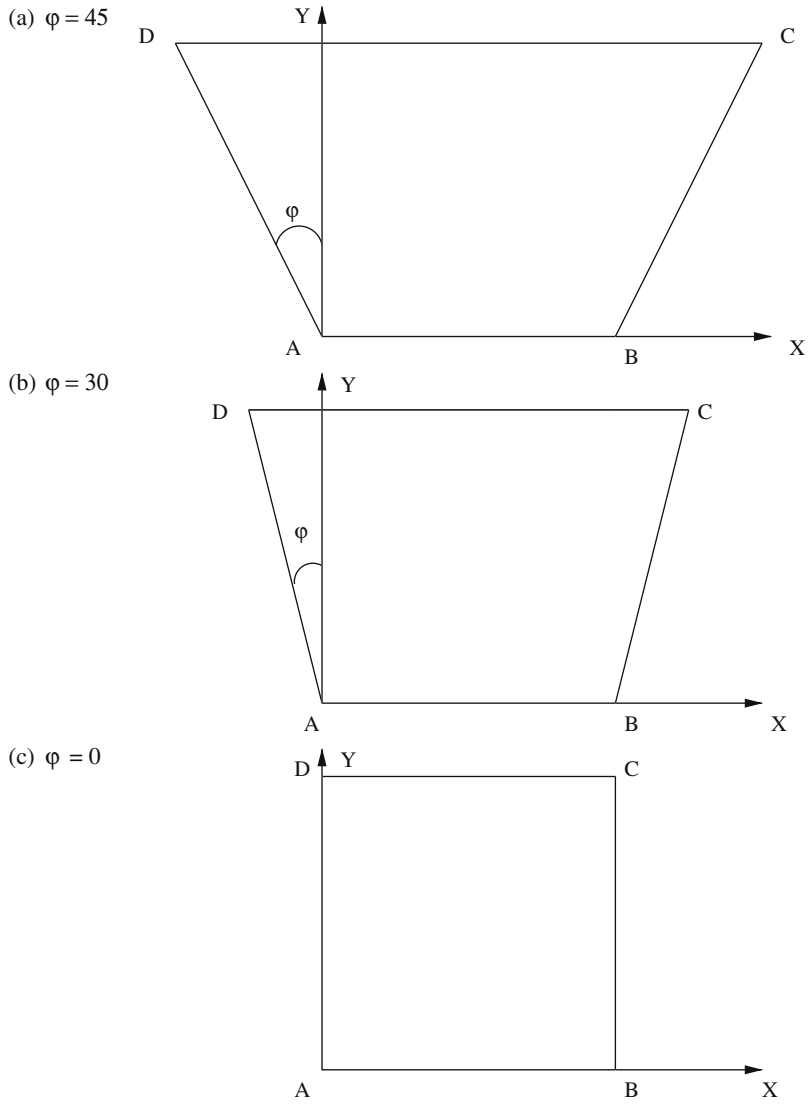

Fig. 1. Schematic diagram of the physical system for (a) $\varphi = 45^\circ$, (b) $\varphi = 30^\circ$, (c) $\varphi = 0^\circ$.

$$\frac{\partial U}{\partial X} + \frac{\partial V}{\partial Y} = 0, \tag{2}$$

$$U\frac{\partial U}{\partial X} + V\frac{\partial U}{\partial Y} = -\frac{\partial P}{\partial X} + Pr\left(\frac{\partial^2 U}{\partial X^2} + \frac{\partial^2 U}{\partial Y^2}\right), \tag{3}$$

$$U\frac{\partial V}{\partial X} + V\frac{\partial V}{\partial Y} = -\frac{\partial P}{\partial Y} + Pr\left(\frac{\partial^2 V}{\partial X^2} + \frac{\partial^2 V}{\partial Y^2}\right) + RaPr\theta, \tag{4}$$

$$U\frac{\partial \theta}{\partial X} + V\frac{\partial \theta}{\partial Y} = \frac{\partial^2 \theta}{\partial X^2} + \frac{\partial^2 \theta}{\partial Y^2}, \tag{5}$$

with the boundary conditions

$$\begin{aligned}
&U = 0, \quad V = 0, \quad \theta = 1, \text{ or } \theta = \sin(\pi X), \quad \forall Y = 0,\ 0 \leqslant X \leqslant 1\\
&U = 0, \quad V = 0, \quad \theta = 0, \quad \forall X\cos(\varphi) + Y\sin(\varphi) = 0,\ 0 \leqslant Y \leqslant 1\\
&U = 0, \quad V = 0, \quad \theta = 0, \quad \forall X\cos(\varphi) - Y\sin(\varphi) = \cos(\varphi),\ 0 \leqslant Y \leqslant 1\\
&U = 0, \quad V = 0, \quad \tfrac{\partial \theta}{\partial Y} = 0, \quad \forall Y = 1,\ -\tan(\varphi) \leqslant X \leqslant 1 + \tan(\varphi)
\end{aligned} \tag{6}$$

Note that, X and Y are dimensionless coordinates varying along horizontal and vertical directions, respectively; U and V are dimensionless velocity components in X and Y directions, respectively; θ is the dimensionless temperature; P is the dimensionless pressure; Ra and Pr are Rayleigh and Prandtl numbers, respectively.

The momentum and energy balance equations (Eqs. (3)–(5)) are solved using the Galerkin finite element method. The continuity equation (Eq. (2)) has been used as a constraint due to mass conservation and this constraint may be used to obtain the pressure distribution. In order to solve Eqs. (3) and (4), we use the penalty finite element method where the pressure P is eliminated by a penalty parameter γ and the incompressibility criteria given by Eq. (2) which results in

$$P = -\gamma\left(\frac{\partial U}{\partial X} + \frac{\partial V}{\partial Y}\right). \tag{7}$$

The continuity equation [Eq. (2)] is automatically satisfied for large values of γ. Typical values of γ that yield consistent solutions are 10^7. Using Eq. (7), the momentum balance equations [Eqs. (3) and (4)] reduce to

$$U\frac{\partial U}{\partial X} + V\frac{\partial U}{\partial Y} = \gamma\frac{\partial}{\partial X}\left(\frac{\partial U}{\partial X} + \frac{\partial V}{\partial Y}\right) + Pr\left(\frac{\partial^2 U}{\partial X^2} + \frac{\partial^2 U}{\partial Y^2}\right), \tag{8}$$

and

$$U\frac{\partial V}{\partial X} + V\frac{\partial V}{\partial Y} = \gamma\frac{\partial}{\partial Y}\left(\frac{\partial U}{\partial X} + \frac{\partial V}{\partial Y}\right) + Pr\left(\frac{\partial^2 V}{\partial X^2} + \frac{\partial^2 V}{\partial Y^2}\right) + RaPr\theta. \tag{9}$$

The system of equations [Eqs. (5), (8) and (9)] with boundary conditions is solved by using Galerkin finite element method ([46]). Expanding the velocity components (U,V) and temperature (θ) using basis set $\{\Phi_k\}_{k=1}^{N}$ as,

$$U \approx \sum_{k=1}^{N} U_k \Phi_k(X,Y), \quad V \approx \sum_{k=1}^{N} V_k \Phi_k(X,Y) \quad \text{and} \quad \theta \approx \sum_{k=1}^{N} \theta_k \Phi_k(X,Y), \tag{10}$$

the Galerkin finite element method yields the following nonlinear residual equations for Eqs. (8), (9) and (5), respectively, at nodes of internal domain Ω:

$$\begin{aligned} R_i^{(1)} = {} & \sum_{k=1}^{N} U_k \int_\Omega \left[\left(\sum_{k=1}^{N} U_k \Phi_k \right) \frac{\partial \Phi_k}{\partial X} + \left(\sum_{k=1}^{N} V_k \Phi_k \right) \frac{\partial \Phi_k}{\partial Y} \right] \Phi_i dXdY \\ & + \gamma \left[\sum_{k=1}^{N} U_k \int_\Omega \frac{\partial \Phi_i}{\partial X} \frac{\partial \Phi_k}{\partial X} dXdY + \sum_{k=1}^{N} V_k \int_\Omega \frac{\partial \Phi_i}{\partial X} \frac{\partial \Phi_k}{\partial Y} dXdY \right] \\ & + Pr \sum_{k=1}^{N} U_k \int_\Omega \left[\frac{\partial \Phi_i}{\partial X} \frac{\partial \Phi_k}{\partial X} + \frac{\partial \Phi_i}{\partial Y} \frac{\partial \Phi_k}{\partial Y} \right] dXdY \end{aligned} \tag{11}$$

$$\begin{aligned} R_i^{(2)} = {} & \sum_{k=1}^{N} V_k \int_\Omega \left[\left(\sum_{k=1}^{N} U_k \Phi_k \right) \frac{\partial \Phi_k}{\partial X} + \left(\sum_{k=1}^{N} V_k \Phi_k \right) \frac{\partial \Phi_k}{\partial Y} \right] \Phi_i dXdY \\ & + \gamma \left[\sum_{k=1}^{N} U_k \int_\Omega \frac{\partial \Phi_i}{\partial Y} \frac{\partial \Phi_k}{\partial X} dXdY + \sum_{k=1}^{N} V_k \int_\Omega \frac{\partial \Phi_i}{\partial Y} \frac{\partial \Phi_k}{\partial Y} dXdY \right] \\ & + Pr \sum_{k=1}^{N} V_k \int_\Omega \left[\frac{\partial \Phi_i}{\partial X} \frac{\partial \Phi_k}{\partial X} + \frac{\partial \Phi_i}{\partial Y} \frac{\partial \Phi_k}{\partial Y} \right] dXdY \\ & - RaPr \int_\Omega \left(\sum_{k=1}^{N} \theta_k \Phi_k \right) \Phi_i dXdY \end{aligned} \tag{12}$$

and

$$\begin{aligned} R_i^{(3)} = {} & \sum_{k=1}^{N} \theta_k \int_\Omega \left[\left(\sum_{k=1}^{N} U_k \Phi_k \right) \frac{\partial \Phi_k}{\partial X} + \left(\sum_{k=1}^{N} V_k \Phi_k \right) \frac{\partial \Phi_k}{\partial Y} \right] \Phi_i dXdY \\ & + \sum_{k=1}^{N} \theta_k \int_\Omega \left[\frac{\partial \Phi_i}{\partial X} \frac{\partial \Phi_k}{\partial X} + \frac{\partial \Phi_i}{\partial Y} \frac{\partial \Phi_k}{\partial Y} \right] dXdY \end{aligned} \tag{13}$$

Bi-quadratic basis functions with three point Gaussian quadrature is used to evaluate the integrals in the residual equations. In Eqs. (11) and (12), the second term containing the penalty parameter (γ) are evaluated with two point Gaussian quadrature (reduced integration penalty formulation, Reddy [46]). The non-linear residual Eqs. (11)–(13) are solved using Newton-Raphson procedure to determine the coefficients of the expansions in Eq. (10). The detailed solution procedure may be found in earlier works ([47,48]).

2.2. Streamfunction and heatfunction

The fluid motion is displayed using the streamfunction (ψ) obtained from velocity components U and V. The relationships between streamfunction, ψ (Batchelor [49]) and velocity components for two-dimensional flows are

$$U = \frac{\partial \psi}{\partial Y} \quad \text{and} \quad V = -\frac{\partial \psi}{\partial X}, \tag{14}$$

which yield a single equation

$$\frac{\partial^2 \psi}{\partial X^2} + \frac{\partial^2 \psi}{\partial Y^2} = \frac{\partial U}{\partial Y} - \frac{\partial V}{\partial X}. \tag{15}$$

Using the above definition of the streamfunction, the positive sign of ψ denotes anti-clockwise circulation and the clockwise circulation is represented by the negative sign of ψ. Expanding the streamfunction (ψ) using the basis set $\{\Phi\}$ as $\psi = \sum_{k=1}^{N} \psi_k \Phi_k(X,Y)$ and the relationship for U and V from Eq. (10), the Galerkin finite element method yields the following linear residual equations for Eq. (15).

$$\begin{aligned} R_i^{s} = {} & \sum_{k=1}^{N} \psi_k \int_\Omega \left[\frac{\partial \Phi_i}{\partial X} \frac{\partial \Phi_k}{\partial X} + \frac{\partial \Phi_i}{\partial Y} \frac{\partial \Phi_k}{\partial Y} \right] dXdY - \int_\Gamma \Phi_i \mathbf{n} \cdot \nabla \psi d\Gamma \\ & + \sum_{k=1}^{N} U_k \int_\Omega \Phi_i \frac{\partial \Phi_k}{\partial Y} dXdY - \sum_{k=1}^{N} V_k \int_\Omega \Phi_i \frac{\partial \Phi_k}{\partial X} dXdY \end{aligned} \tag{16}$$

The no-slip condition is valid at all boundaries as there is no cross flow, hence $\psi = 0$ is used as residual equations at the nodes for the boundaries. The bi-quadratic basis function is used to evaluate the integrals in Eq. (16) and ψs are obtained by solving the residual Eq. (16).

The heat flow within the enclosure is displayed using the heatfunction (Π) obtained from conductive heat fluxes $\left(-\frac{\partial \theta}{\partial X}, -\frac{\partial \theta}{\partial Y}\right)$ as well as convective heat fluxes $(U\theta, V\theta)$. The heatfunction satisfies the steady energy balance equation (Eq. (5)) ([25]) such that

$$\begin{aligned} \frac{\partial \Pi}{\partial Y} &= U\theta - \frac{\partial \theta}{\partial X}, \\ -\frac{\partial \Pi}{\partial X} &= V\theta - \frac{\partial \theta}{\partial Y}, \end{aligned} \tag{17}$$

which yield a single equation

$$\frac{\partial^2 \Pi}{\partial X^2} + \frac{\partial^2 \Pi}{\partial Y^2} = \frac{\partial}{\partial Y}(U\theta) - \frac{\partial}{\partial X}(V\theta). \tag{18}$$

Using the above definition of the heatfunction, the positive sign of Π denotes anti-clockwise heat flow and the clockwise heat flow is represented by the negative sign of Π. Expanding the heatfunction (Π) using the basis set $\{\Phi\}$ as $\Pi = \sum_{k=1}^{N} \Pi_k \Phi_k(X,Y)$ and the relation for U,V and θ from Eq. (10), the Galerkin finite element method yields the following linear residual equations for Eq. (18).

$$\begin{aligned} R_i^{h} = {} & \sum_{k=1}^{N} \Pi_k \int_\Omega \left[\frac{\partial \Phi_i}{\partial X} \frac{\partial \Phi_k}{\partial X} + \frac{\partial \Phi_i}{\partial Y} \frac{\partial \Phi_k}{\partial Y} \right] dXdY - \int_\Gamma \Phi_i \mathbf{n} \cdot \nabla \Pi d\Gamma \\ & + \sum_{k=1}^{N} U_k \int_\Omega \left(\sum_{k=1}^{N} \theta_k \Phi_k \right) \Phi_i \frac{\partial \Phi_k}{\partial Y} dXdY \\ & + \sum_{k=1}^{N} \theta_k \int_\Omega \left(\sum_{k=1}^{N} U_k \Phi_k \right) \Phi_i \frac{\partial \Phi_k}{\partial Y} dXdY \\ & - \sum_{k=1}^{N} V_k \int_\Omega \left(\sum_{k=1}^{N} \theta_k \Phi_k \right) \Phi_i \frac{\partial \Phi_k}{\partial X} dXdY \\ & - \sum_{k=1}^{N} \theta_k \int_\Omega \left(\sum_{k=1}^{N} V_k \Phi_k \right) \Phi_i \frac{\partial \Phi_k}{\partial X} dXdY \end{aligned} \tag{19}$$

The residual equation (Eq. (19)) is further supplemented with various Dirichlet and Neumann boundary conditions in order to obtain an unique solution of Eq. (18). Neumann boundary conditions for Π are obtained for isothermal (hot or cold) or sinusoidally heated wall as derived from Eq. (17) and the normal derivatives $(\mathbf{n} \cdot \nabla \Pi)$ are specified as follows:

(a) for bottom wall

$$\begin{aligned} &\mathbf{n} \cdot \nabla \Pi = 0 \text{ (uniform heating)} \\ &= \pi \cos \pi X \text{ (sinusoidal heating)} \end{aligned} \tag{20}$$

and

(b) for vertical wall

$$\mathbf{n} \cdot \nabla \Pi = 0 \text{ (cooling)} \tag{21}$$

The top insulated wall may be represented by Dirichlet boundary condition as obtained from Eq. (17) which is simplified into $\frac{\partial \Pi}{\partial X} = 0$ for an adiabatic wall. A reference value of Π is assumed as 0 at the edge D (Fig. 1a–c) and hence $\Pi = 0$ is valid for $Y = 1, \forall X$. It may be noted that, the unique solution of Eq. (18) is strongly dependent on the non-homogeneous Dirichlet conditions. It may be noted that most of earlier works [38,27] are limited within two adiabatic walls where Dirichlet boundary condition is either 0 or Nu at the adiabatic walls. Current work is based on the situations of differential heating of walls and Dirichlet conditions for Π have been obtained based on heat flux balance i.e., the total heat gained by the cold wall equals the total heat loss from the hot wall. Therefore, following Dirichlet boundary conditions have been derived.

$$\Pi = \frac{\overline{Nu_l}}{\cos\varphi} \text{ at edge A} = -\frac{\overline{Nu_r}}{\cos\varphi} \text{ at edge B} \tag{22}$$

The evaluation of average Nusselt numbers for the left and right walls ($\overline{Nu_l}$ and $\overline{Nu_r}$) are discussed in next section.

The sign of heatfunction needs special mention. The solution of heatfunction (Poisson equation) is strongly dependent on non-homogeneous Dirichlet boundary conditions and the sign of heatfunction is governed by the sign of 'non-homogeneous' Dirichlet condition at the junction of hot and cold walls. The heat flow always occurs from the hot to cold regime and the positive sign of 'non-homogeneous' Dirichlet condition denotes the anti-clockwise heat flow. It may also be noted that signs of streamfunction and heatfunction are identical for the convection dominated heat flows.

2.3. Nusselt numbers

The heat transfer coefficient in terms of the local Nusselt number (Nu) is defined by

$$Nu = -\frac{\partial \theta}{\partial n}, \tag{23}$$

where n denotes the normal direction on a plane. The normal derivative is evaluated by the bi-quadratics basis set in $\xi - \eta$ domain. The local Nusselt numbers at bottom wall (Nu_b), left wall (Nu_l) and right wall (Nu_r) are defined as

$$Nu_b = \sum_{i=1}^{9} \theta_i \frac{\partial \Phi_i}{\partial Y}, \tag{24}$$

$$Nu_l = \sum_{i=1}^{9} \theta_i \left(\cos\varphi \frac{\partial \Phi_i}{\partial X} + \sin\varphi \frac{\partial \Phi_i}{\partial Y} \right). \tag{25}$$

and

$$Nu_r = -\sum_{i=1}^{9} \theta_i \left(\cos\varphi \frac{\partial \Phi_i}{\partial X} - \sin\varphi \frac{\partial \Phi_i}{\partial Y} \right). \tag{26}$$

The average Nusselt numbers at the bottom, left and right walls are

$$\overline{Nu_b} = \frac{\int_0^1 Nu_b dX}{X|_0^1} = \int_0^1 Nu_b dX, \tag{27}$$

$$\overline{Nu_l} = \cos\varphi \int_0^{\frac{1}{\cos\varphi}} Nu_l ds_1, \tag{28}$$

and

$$\overline{Nu_r} = \cos\varphi \int_0^{\frac{1}{\cos\varphi}} Nu_r ds_2, \tag{29}$$

where ds_1 and ds_2 are the small elemental lengths along the left and right walls, respectively. Note that, $\overline{Nu_l} = \overline{Nu_r} = \overline{Nu_s}$ may be assumed due to symmetry in boundary conditions at side walls.

3. Results and discussion

3.1. Numerical tests

The computational grid in the trapezoidal domain is generated via mapping the triangular domain into square domain in $\xi - \eta$ coordinate system as shown in Fig. 2 and the procedure

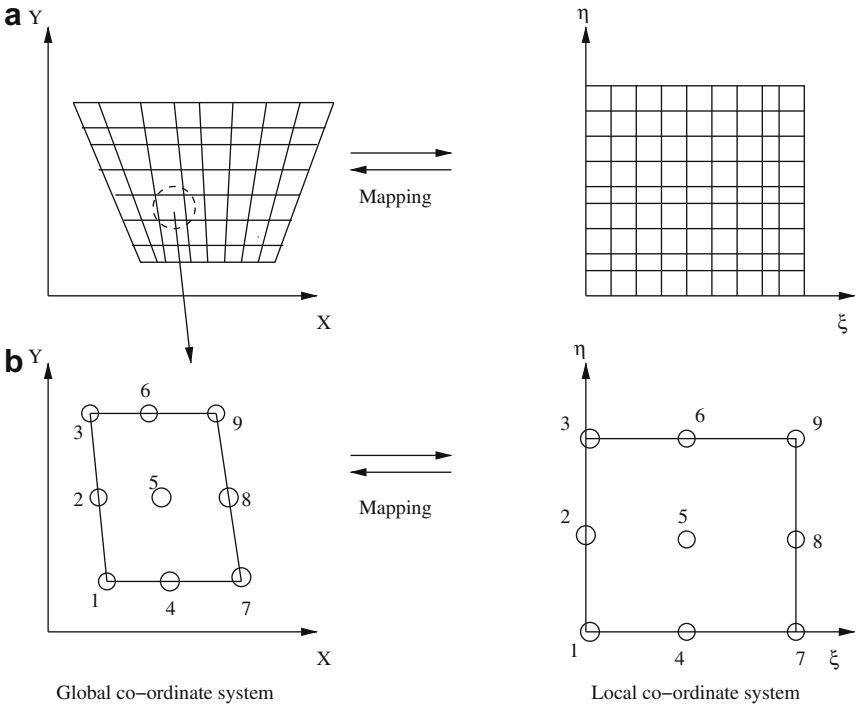

Fig. 2. (a) The mapping of trapezoidal domain to a square domain in $\xi - \eta$ coordinate system and (b) the mapping of an individual element to a single element in $\xi - \eta$ coordinate system.

is outlined in Appendix A. The computational domain in $\xi - \eta$ coordinates (Fig. 2) consists of 20×20 bi-quadratic elements which correspond to 41×41 grid points. The bi-quadratic elements with lesser number of nodes smoothly capture the nonlinear variations of the field variables which are in contrast with finite difference/finite volume solutions available in literature [21].

In the current investigation, Gaussian quadrature based finite element method provides the smooth solutions at the interior domain including the corner regions as evaluation of residuals depends on the interior Gauss points and thus the effect of corner nodes are less profound in the final solution as discussed by earlier researchers [47,48]. In general, the Nusselt numbers for finite difference/finite volume based methods are calculated at any surface using some interpolation functions [21] which are now avoided in the current work. The present finite element method based approach offers special advantage on evaluation of local Nusselt number at the left, right and bottom walls as the element basis functions have been used to evaluate the heat flux and Nusselt numbers.

Current finite element based solutions on streamfunctions and isotherms have been compared with finite volume based solutions for trapezoidal enclosures [21] and the solutions are in well agreement. It may be noted that current solution is based on 20×20 bi-quadratic elements whereas the earlier work [21] is based on 60×60 control volume grid.

The results of heatlines are found to be in well agreement with the earlier work [38] for a square enclosure ($\varphi = 0^\circ$) filled with air ($Pr = 0.71$) subjected to hot left wall and cold right wall in presence of insulated horizontal walls at $Ra = 10^5$. Till date, heatlines have not been reported for irregular geometries. However, heatlines are perpendicular to the isothermal surface and they are smooth curves for the conduction dominant heat transfer. These features are clearly seen in Fig. 3a–c.

3.2. Case 1: uniform heating of bottom wall

Figs. 3–6 illustrate streamlines, isotherms and heatlines for $Pr = 0.026 - 1000$ and $Ra = 10^3 - 10^5$ during uniform heating of bottom wall in presence of cold side walls. In general, fluid rise up from the middle portion of the bottom wall and flow down along two cold vertical walls forming two symmetric rolls with clockwise and anticlockwise rotations inside the cavity. For $Ra = 10^3, Pr = 0.026$ (Fig. 3), the magnitudes of streamfunction are considerably smaller and the heat transfer is primarily due to conduction. For $Ra = 10^3$ with $\varphi = 45^\circ$, the isotherms with $\theta = 0.1 - 0.4$ occur symmetrically near the side walls of the enclosure (Fig. 3a). The other isotherms with $\theta \geqslant 0.5$ are smooth curves symmetric with respect to vertical symmetric line at the center. For $\varphi = 30^\circ$, the temperature contours with $\theta = 0.1 - 0.3$ occur symmetrically near the side walls of the enclosure (Fig. 3b). The other isotherms with $\theta \geqslant 0.4$ are smooth curves symmetric with respect to central symmetric line. For $\varphi = 0^\circ$ (square cavity), the isotherms with $\theta = 0.1$ occur symmetrically along the side walls and isotherms with $\theta \geqslant 0.2$ are smooth curves symmetric with respect to the vertical symmetric line (Fig. 3c). It is interesting to note that the stronger convection, however small, occurs for $\varphi = 45^\circ$ and 30°. The central regime attains the largest temperature for $\varphi = 45^\circ$.

The temperature distribution for various φ in trapezoidal enclosures can further be explained with distribution of heat energy which is governed by heatfunctions or heatlines. Heatlines are shown in panels of Fig. 3a–c. Heatlines illustrate that the heat energy from the bottom wall symmetrically distributed to side walls irrespective of φ especially for smaller Ra. It is important to note that, the two bottom corner edges have infinite heat flux as the cold wall is directly in contact with the hot bottom wall. Note that, the signs of heatfunctions are dependent on boundary conditions at two bottom corners. Our sign convention is based

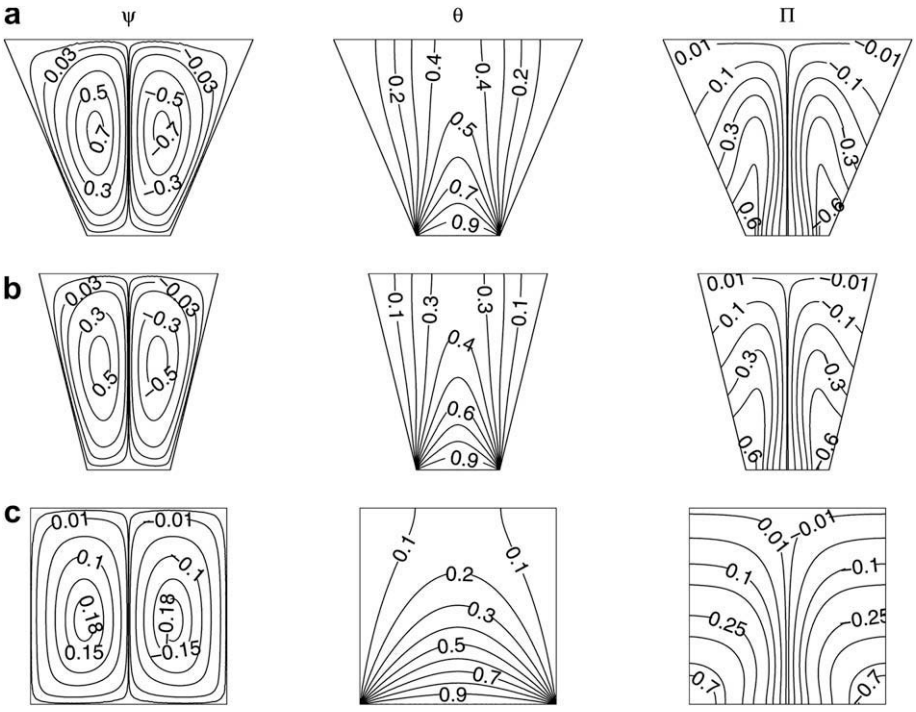

Fig. 3. Streamfunction (ψ), temperature (θ), and heatfunction (Π) contours for uniform bottom heating, $\theta(X, 0) = 1$ with $Pr = 0.026$ and $Ra = 10^3$: (a) $\varphi = 45^\circ$, (b) $\varphi = 30^\circ$ and (c) $\varphi = 0^\circ$.

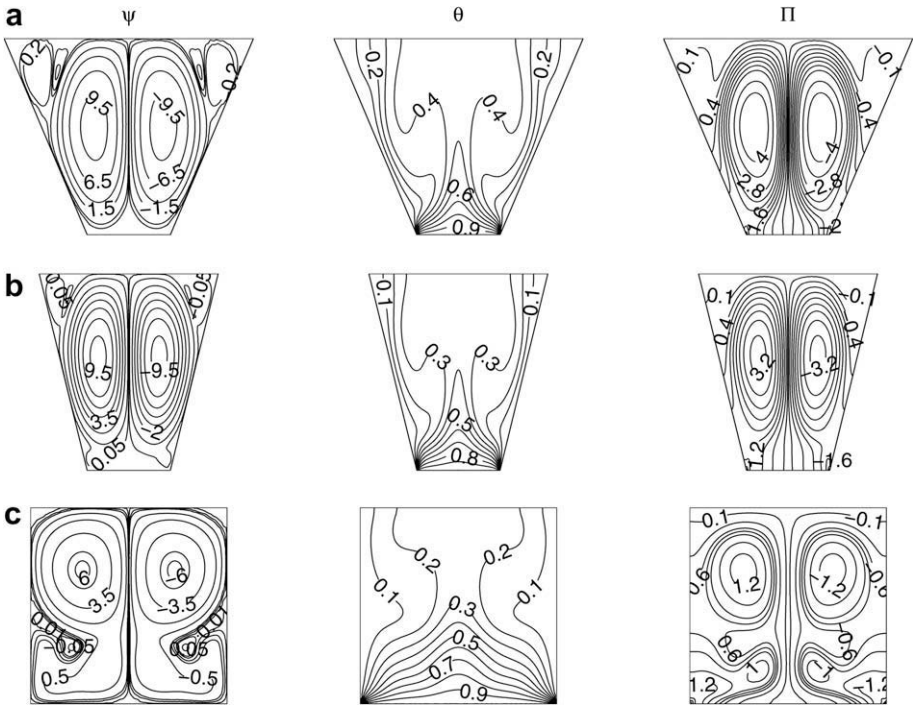

Fig. 4. Streamfunction (ψ), temperature (θ), and heatfunction (Π) contours for uniform bottom heating, $\theta(X,0)=1$ with $Pr=0.026$ and $Ra=10^5$: (a) $\varphi=45^\circ$, (b) $\varphi=30^\circ$ and (c) $\varphi=0^\circ$.

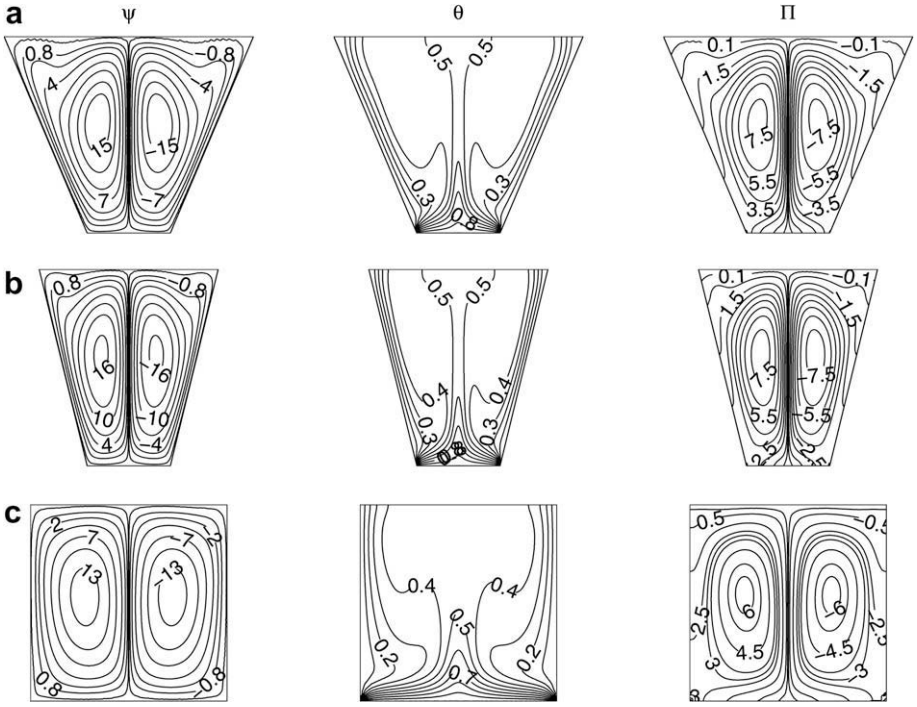

Fig. 5. Streamfunction (ψ), temperature (θ), and heatfunction (Π) contours for uniform bottom heating, $\theta(X,0)=1$ with $Pr=0.7$ and $Ra=10^5$: (a) $\varphi=45^\circ$, (b) $\varphi=30^\circ$ and (c) $\varphi=0^\circ$.

on the fact that the heat flow occurs from the hot to cold wall, and the positive heatfunction corresponds to anticlockwise heat flow. It may also be noted that, $\frac{\overline{Nu}_l}{\cos\varphi}$ or $-\frac{\overline{Nu}_r}{\cos\varphi}$ denotes the total or cumulative heat flux at two bottom corner points and therefore, the magnitudes of heatfunctions decrease from the bottom edges to the central symmetric line where no heat flux condition is valid due to symmetric boundary conditions for temperature. Note that, heatlines are perpendicular towards the side walls indicating the normal heat flux along the wall. It may also be noted that the straight normal heat flux lines to the side walls indicate the dominant conduction mode. The parallel heatlines which are also normal to the walls for any φ is expected for dominant conduction mode and these features are validated for the first time in this work.

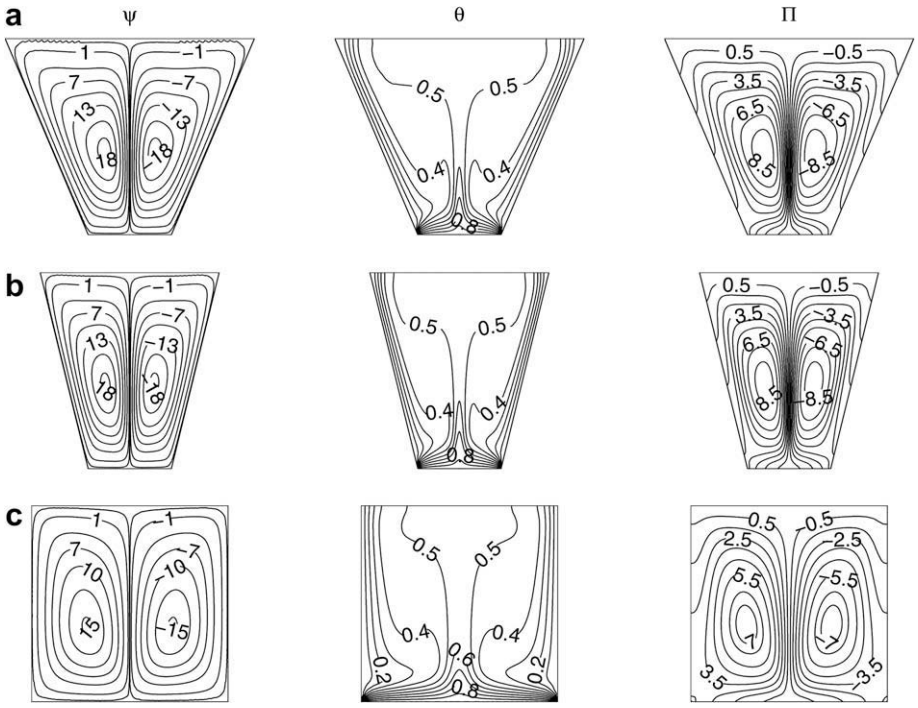

Fig. 6. Streamfunction (ψ), temperature (θ), and heatfunction (Π) contours for uniform bottom heating, $\theta(X,0)=1$ with $Pr=1000$ and $Ra=10^5$: (a) $\varphi=45^\circ$, (b) $\varphi=30^\circ$ and (c) $\varphi=0^\circ$.

It is also interesting to note that, the heatfunction (Π) at the bottom corner point for $\varphi=0^\circ$ is larger than those for $\varphi=45^\circ$ and 30°. It is observed that the heatlines near the bottom portion of side walls are more dense for $\varphi=45^\circ$ whereas the heatlines are less dense for $\varphi=0^\circ$ (square cavity). The dense heatlines further indicate enhanced rate of heat transfer from the bottom to the side walls. Therefore isotherms with $\theta=0.1-0.4$ are shifted towards the side wall for $\varphi=45^\circ$. It is also interesting to observe that, heat transport at the top portion of the cavity for $\varphi=45^\circ$ and $\varphi=30^\circ$ is higher compared to $\varphi=0^\circ$ based on values of Π. Therefore, temperature at the top portion is larger for $\varphi=45^\circ$ and 30°. As the heat transfer rate is quite large at the corners of the bottom wall, the thermal boundary layer was found to develop near bottom edges, and the thickness of boundary layer is larger at the top portion of the cold wall signifying less heat transfer to the top portion. The thermal boundary layer thickness is larger for $\varphi=0^\circ$ as smaller values of Π are observed at the top portion. The stratification of temperature contours occur near the center of the bottom wall as almost vertical heatlines occur near that regime.

At larger $Ra(Ra=10^5)$, the effect of buoyancy force is stronger compared to viscous forces and the intensity of fluid motion has been increased as indicated by larger magnitudes of streamfunctions (Fig. 4). The enhanced convection causes larger heat energy to flow from the bottom wall to the top portion of the vertical wall and a large regime of top portion of the cavity remains at uniform temperature for $\varphi=45^\circ$ and 30°. It is interesting to observe that the stratification zone of temperature at the central vertical line near the bottom wall is suppressed for $Ra=10^5$ due to enhanced convection whereas the stratification zone is larger for $Ra=10^3$. It may be noted that the stratification zone of temperature at bottom is thicker for $\varphi=0^\circ$ due to less intense circulation near the top portion of the cavity. It is also observed that the isotherms are compressed strongly towards the side walls for $Ra=10^5$ especially with $\varphi=45^\circ$ and 30°. The isotherms with $\theta\leqslant 0.4, \theta\leqslant 0.3, \theta\leqslant 0.2$ are compressed near the side walls of the enclosure for $\varphi=45^\circ, 30^\circ$ and 0°, respectively. It is also observed that isotherms for $\varphi=45^\circ$ are more distorted (Fig. 4a) compared to 30° (Fig. 4b) and 0° (Fig. 4c). The shapes of streamlines are found almost circular except near the side wall. It is interesting to observe that, for $\varphi=45^\circ$ and 30°, symmetric multiple circulations near top corners appear whereas weak secondary circulation also occur near the center of the side walls for $\varphi=0^\circ$.

Two types of heatlines are found: one indicating heat transfer from the hot wall to the cold side walls and the other indicating heat flow/circulations due to fluid circulation cells. Heatlines near the top portion of the side walls are oscillatory due to secondary circulation for $\varphi=45^\circ$ and 30°. It is interesting to observe that the heatlines are quite dense near the central regime for $\varphi=45^\circ$ and 30° and this implies enhanced heat transfer or thermal mixing near the central to top portion of the cavity. It is also interesting to note that the convective transport of heat also suppresses isotherms near the central part of side walls for $\varphi=45^\circ$ and 30°. In contrast, the isotherms are less dense near the central regime of the side walls for $\varphi=0^\circ$ and thus the boundary layer thickness is large near the central regime of the side wall especially for $\varphi=0^\circ$. The larger thickness of thermal boundary layer also corresponds to less dense heatlines at the central regime of side walls for $\varphi=0^\circ$ (Fig. 4c). It may also be noted that the significant convection causes distortion of heatlines especially near the side walls as compared with conduction dominant heat transfer (see Fig. 3). It is also interesting to observe that the shape of heatlines near the core is identical with the streamlines, signifying the convection dominant heat flow due to large intensity of circulations as shown with large values of streamfunctions. The weak secondary circulation cells of heatlines near the bottom wall are due to secondary circulations as seen in Fig. 4c.

At a larger $Pr(Pr=0.7)$ with $Ra=10^5$, the intensity of flow circulations have been increased irrespective of φ as seen from Fig. 5a–c. Although the streamlines are circular or elliptical near the core, but the streamlines near the wall is almost parallel to wall exhibiting large intensity of flow. It may be noted that, $|\psi|_{max}=15, 16$ and 13 for $\varphi=45^\circ, 30^\circ$ and 0°, respectively, whereas the maximum value of the streamfunctions are lesser

for $Pr = 0.026$ and $Ra = 10^5$ as seen in Fig. 4a–c. It is also interesting to observe that multiple circulations are completely absent for $Pr = 0.7$ and $Ra = 10^5$. Due to enhanced flow circulations, the isotherms are highly compressed near the side walls except near the bottom portion especially for $\varphi = 45^\circ$ and 30°. The boundary layers are found to develop at two corners of the bottom wall for all the angles. It is also interesting to observe that a large regime at the core of the cavity is maintained at $\theta = 0.5$.

The thermal energy transport is further analyzed with heatlines. Similar to $Pr = 0.026$ and $Ra = 10^5$, two types of heatlines are observed. The enhanced thermal mixing near the central regime is attributed to the highly dense heatlines especially for $\varphi = 45^\circ$ and 30°. The dense heatlines consist of the heatlines emanating from the heated bottom wall and other lines as parts of convective circulation of heat. Therefore, the enhanced thermal mixing near the core leads to uniform temperature $\theta = 0.5$. Similar phenomena was also observed for $Pr = 0.026$ and $Ra = 10^5$, but the intensity of heat transport is lesser for $Pr = 0.026$. It may be noted that, $|\Pi|_{max}$ near the core is around 4 for $\varphi = 45^\circ$ and 3.2 for $\varphi = 30^\circ$ corresponding to $Pr = 0.026$ and $Ra = 10^5$ (Fig. 4a and b) whereas those are around 7.5 for $\varphi = 45^\circ$ and 30° for $Pr = 0.7$ and $Ra = 10^5$ (Fig. 5a and b). The significant amount of thermal mixing does occur for $\varphi = 0^\circ$ as $|\Pi|_{max}$ is around 6 in the core regime for $Pr = 0.7$. Furthermore, the multiple circulation cells are absent for $Pr = 0.7$ whereas multiple heat circulation loops were observed for $Pr = 0.026$ (see Fig. 4c). Similar to Fig. 4a–c, heatlines are less dense near bottom corners irrespective of φs and boundary layers start developing from corner points. The large temperature gradient near the side walls are due to significant number of heatlines with a large variation of heatfunctions as seen in Fig. 5a–c whereas the heatlines along the side walls are less dense leading to less thermal gradient for $Pr = 0.026$.

At $Pr = 1000$ and $Ra = 10^5$ (Fig. 6), the intensity of flow circulations are enhanced as seen from values of streamfunctions. In all cases, the streamlines near the wall take the shape of the container and that signifies enhanced mixing effects. A larger regime near the center corresponds to $\theta = 0.5$ irrespective of all φs. The isotherms with $\theta \leqslant 0.4$ are highly compressed near the side walls and isotherms with $\theta \geqslant 0.6$ are also confined within a small regime near the bottom wall. Similar to $Pr = 0.7$ (Fig. 5), boundary layers are also formed along the side walls. The heatlines are highly dense at the central regime and $|\Pi|_{max}$ is around 8.5 for $\varphi = 45^\circ$ and 30° and that is 7 for $\varphi = 0^\circ$. The enhanced thermal mixing due to convection as well as heat transport from the bottom wall leads to uniform temperature near the central regime. Also, the significant number of heatlines are observed along the side walls leading to large thermal gradient for $\varphi = 45^\circ$ and 30°. In contrast, the heatlines are less dense along the side vertical walls for $\varphi = 0^\circ$ and therefore, the boundary layer thickness is larger as seen in Fig. 6c. Common to all cases, $|\Pi|$ varies within 0-2.5 along the bottom wall and thus the large heat transfer results in compression of isotherms along the bottom wall.

3.3. Case 2: non-uniform heating of bottom wall

Figs. 7 and 8 illustrate streamlines, isotherms and heatlines for $Pr = 0.026$ and $Pr = 0.7$, respectively, for high Rayleigh number ($Ra = 10^5$) during non-uniform heating of the bottom wall. Fig. 7a–c illustrate that streamlines are qualitatively similar to those for uniform heating case as seen in Fig. 4a–c. The overall intensity of circulations was found to be higher for uniform heating situation due to larger heating effects for all φs. The isotherms for non-uniform heating cases also look qualitatively similar to those of uniform heating cases. Due to overall less heating effects, the temperature (θ) at the central regime varies within 0.3–0.4 for $\varphi = 45^\circ$, 0.2–0.3 for $\varphi = 30^\circ$ and 0.1–0.2 for $\varphi = 0^\circ$. The heatlines illustrate similar features that were observed for uniform heating cases. The heat transfer in the central regime is mostly dominated by convection especially for $\varphi = 45^\circ$ and 30°. The heat transfer in corner regimes at the bottom wall is dominated by conduction irrespective of φs. It is also observed that, the primary and secondary heatline cells due to multiple flow circulation cells are observed for the square domain ($\varphi = 0^\circ$). The less intense heating effects near the central regime are attributed by less dense heat-

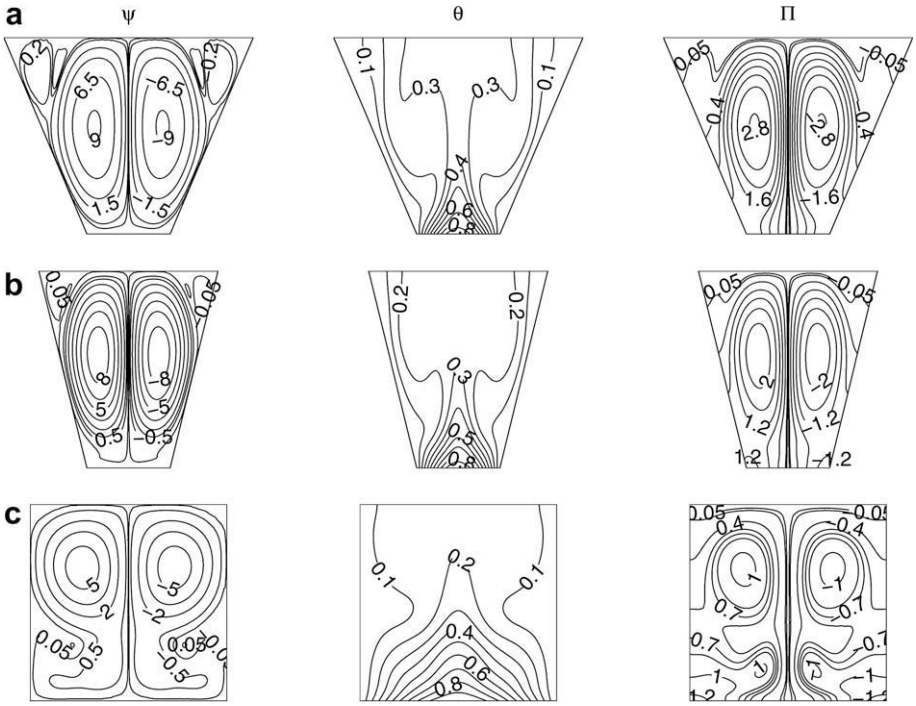

Fig. 7. Streamfunction (ψ), temperature (θ), and heatfunction (Π) contours for non-uniform bottom heating, $\theta(X, 0) = \sin(\pi x)$ with $Pr = 0.026$ and $Ra = 10^5$: (a) $\varphi = 45^\circ$, (b) $\varphi = 30^\circ$ and (c) $\varphi = 0^\circ$.

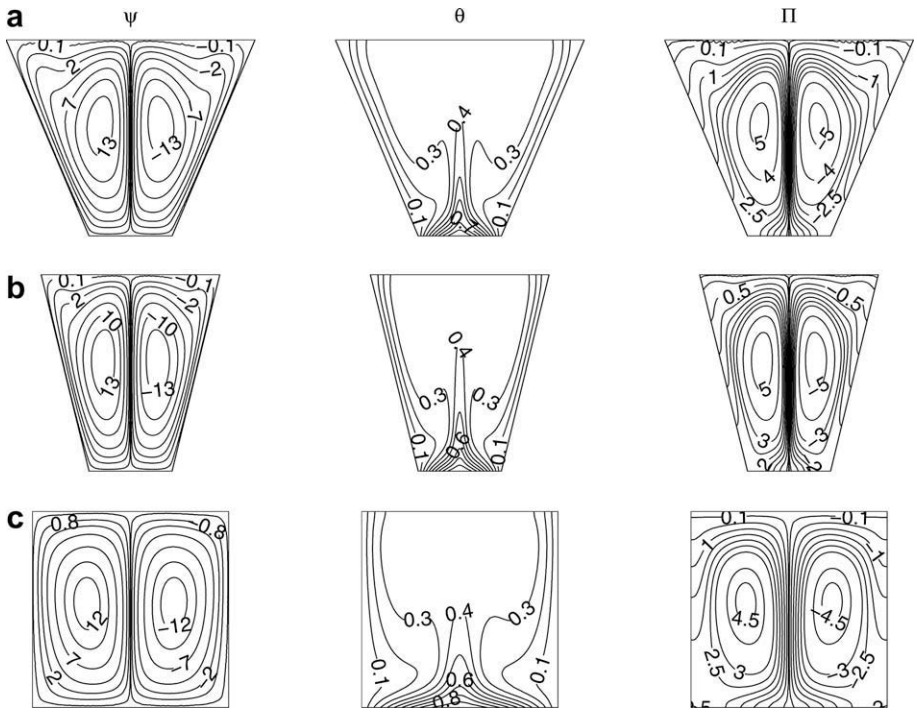

Fig. 8. Streamfunction (ψ), temperature (θ), and heatfunction (Π) contours for non-uniform bottom heating, $\theta(X,0) = \sin(\pi x)$ with $Pr = 0.7$ and $Ra = 10^5$: (a) $\varphi = 45^\circ$, (b) $\varphi = 30^\circ$ and (c) $\varphi = 0^\circ$.

lines due to non-uniform heating effects. It may be noted that $|\Pi|_{max}$ is around 2.8 for $\varphi = 45^\circ$, 2.2 for $\varphi = 30^\circ$ and 1 for $\varphi = 0^\circ$ at the core due to convective effects whereas $|\Pi|_{max}$ is around 4 for $\varphi = 45^\circ$, 3.2 for $\varphi = 30^\circ$ and 1.2 for $\varphi = 0^\circ$ at the core for uniform heating.

Fig. 8 illustrates the streamlines, isotherms and heatlines for $Pr = 0.7$ and $Ra = 10^5$ for non-uniform heating case. The streamlines, isotherms and heatlines for non-uniform heating case are qualitatively similar to those of uniform heating case (see Figs. 5a–c and 8a–c). Although the intensity of flow circulations is found to be stronger than that for $Pr = 0.026$, but the intensity of thermal mixing near the core is less compared to the uniform heating case for $Pr = 0.7$ based on magnitudes of heatfunctions. The temperature (θ) near the core is around 0.4 with non-uniform heating case whereas θ is around 0.5 for uniform heating case (see Figs. 5 and 8).

3.4. Heat transfer rates: local and average Nusselt numbers

Fig. 9a and b illustrate the local Nusselt number vs distance for the bottom and side walls, respectively, for $Pr = 0.7$ and $Ra = 10^5$. The heat transfer rates are shown for $Ra = 10^5$ as convection is dominant for large Ra. Fig. 9a illustrates the local heat transfer rate (Nu_b) for the bottom wall. It is observed that the heat transfer rate is maximum near the edge of the wall and the rate is minimum near the center of the wall irrespective of all angles (φ) for uniform heating of the bottom wall (case 1). It is also interesting to observe that the heat transfer rates (Nu_b) for $\varphi = 45^\circ$ and $\varphi = 30^\circ$ are almost identical whereas Nu_b is larger for $\varphi = 0^\circ$ except near the edges of the wall. It is observed that the thermal gradient is minimum at the center of the bottom wall as seen from the dispersed isotherm contours at the center of the wall irrespective of φ. The larger heat transfer rate for $\varphi = 0^\circ$ occurs due to highly compressed isotherms as seen from Fig. 5c.

On the other hand, the heat transfer rates show oscillatory distribution for non-uniform heating of the bottom wall (Fig. 9a). It is interesting to observe that Nu_b distribution is almost identical for

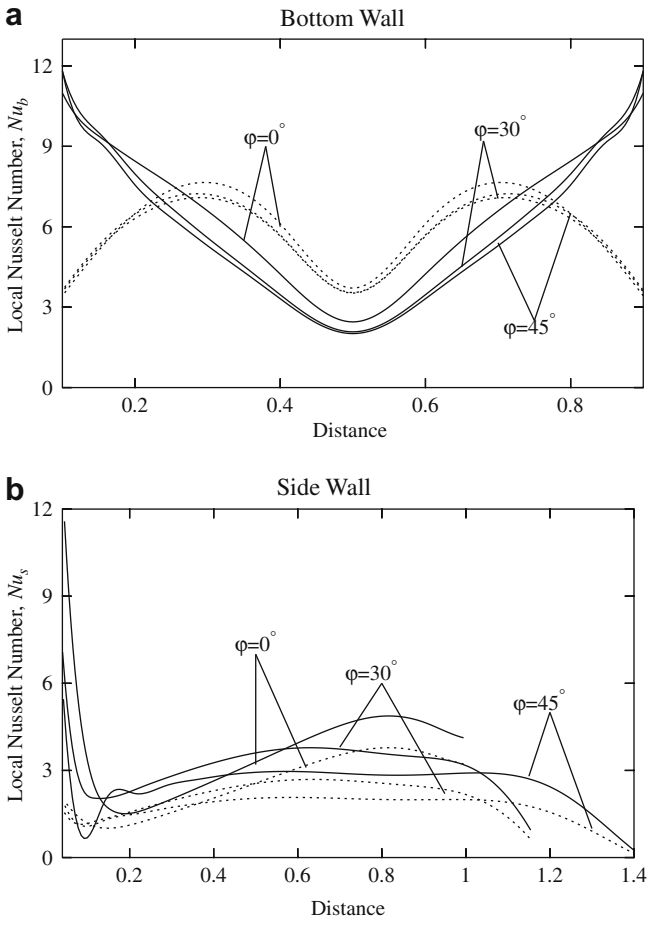

Fig. 9. Variations of local Nusselt numbers ((a) Nu_b; (b) Nu_s) with distance for $Pr = 0.7$ and $Ra = 10^5$ in presence of uniform heating (—) and non-uniform heating (---) of bottom walls.

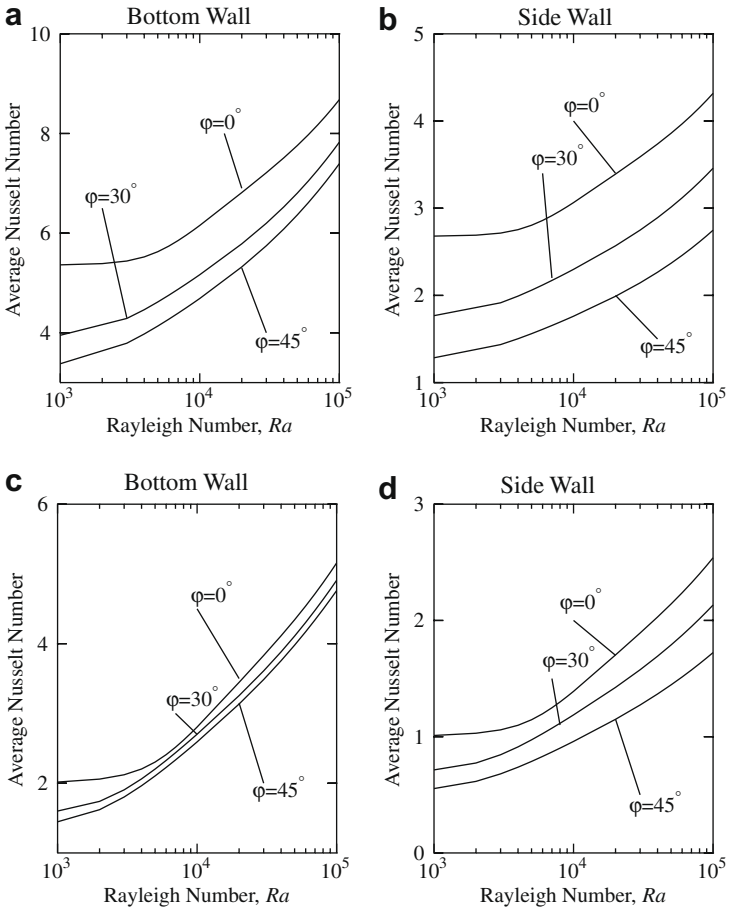

Fig. 10. Average Nusselt number vs Rayleigh number for uniform heating ((a) and (b)) and non-uniform heating ((c) and (d)) of bottom wall with $Pr = 0.7$.

$\varphi = 45^\circ$ and 30°. A slight increase in Nu_b for $\varphi = 0^\circ$ at the central regime is observed. A general trend for Nu_b is to note that the maxima in heat transfer rate is observed at distance of 0.3 and 0.7. The spatial maxima in Nu_b is due to largely compressed isotherm. The local minima of Nu_b for $\varphi = 45^\circ$ and 30° at the center is smaller than that for 0° and this is due to the largely dispersed isotherms for larger φs as seen in Fig. 8a and b. It is also interesting to observe that the heat transfer rate at the central regime is larger with non-uniform heating effects. This may be explained based on heatlines. It is observed that heatlines with $|\Pi| = 0 - 2$ are confined within a narrow regime at the center of the bottom wall for non-uniform heating case whereas $|\Pi| = 0 - 2$ are spread in a large regime for uniform heating case (see Figs. 4a–c and 8a–c). Very few heatlines are present near the bottom corner for non-uniform heating case and thus Nu_b is smaller than that with uniform heating case.

Fig. 9b illustrates the local heat transfer rates for the side wall (Nu_s). It is observed that the local Nusselt number (Nu_s) is largest at the bottom edge of the side wall, and thereafter that decreases sharply upto a point which is very near to the bottom edge. Afterwords, Nu_s increases upto a point near to the top wall and it is interesting to observe that Nu_s decreases with distance near to the top wall. The similar qualitative trend is observed for both the uniform and non-uniform heating of the bottom wall. The boundary layer starts to form at the bottom edge of the side wall and the boundary layer thickness is quite large near the bottom wall for all φs. Due to large intensity of convection at $Ra = 10^5$, the thickness of boundary layers are quite small at the middle portion of side walls. The boundary layer thickness is found to be larger near the top portion and therefore, Nu_s is found to be smaller near that regime. It may be mentioned that the larger degree of compression of isotherms for uniform heating case results in larger Nu_s. It may also be noted that Nu_s is quite large near to the bottom wall end where dominant conductive heat transport occurs.

Fig. 10a–d illustrate that average Nusselt number increases with Rayleigh number monotonically irrespective of φs. Fig. 10a and b illustrate variations for uniform heating case (case 1) and Fig. 10c and d illustrate variations for non-uniform heating case (case 2). It is observed that heat transfer rate is largest for $\varphi = 0^\circ$. This may be explained based on local Nusselt number plots as shown in Fig. 9a and b. It was interesting to observe that Nu_b at the middle portion of the bottom wall for $\varphi = 0^\circ$ is largest for both uniform and non-uniform heating effects. It was also observed that Nu_l is largest near the bottom corner of the side walls for $\varphi = 0^\circ$. Variations of average Nusselt numbers with inclination angles are smaller due to non-uniform heating effect. The magnitudes of average Nusselt numbers are also found to be lesser for non-uniform heating case.

4. Conclusion

Heatlines are extensively analyzed to demonstrate the heat flow for various patterns of heating of bottom wall with various shapes of trapezoidal cavities. Heatlines are uniquely determined from heatfunctions which are obtained via solving Poisson equation. Heatfunctions and streamfunctions alongwith velocity and temperature fields are solved using Galerkin finite element method. Heatfunctions are strongly dependent on non-homogeneous Dirichlet boundary conditions at the junctions between bottom and side walls. The non-homogeneous Dirichlet conditions are obtained from average Nusselt numbers which further ensure that heatlines satisfy the energy balance equations. The detailed analy-

sis on solutions of heatfunctions with this unique situation on hot–cold wall junction within a series of trapezoidal cavities are done first time in this work.

Initially, the heatlines are analyzed for $Pr = 0.026$ with $Ra = 10^3$ which corresponds to conduction dominant heat transport as seen from very weak flow circulations. The heatlines are found to be an useful tool to visualize the conductive transport. It is clearly observed that heatlines are perpendicular to the side walls and the bottom wall. The heat is symmetrically distributed to the cold side walls and the heatlines are tangential to the adiabatic wall. It is also observed that each heatline connects the hot bottom wall and side wall and they are parallel to each other in presence of dominant conduction mode. These features are common to both uniform and non-uniform heating of bottom wall. Heatlines are also analyzed with larger $Ra(Ra = 10^5)$ both for small and large values of $Pr(Pr = 0.026 - 1000)$. It is observed that the multiple flow circulations occur at $Pr = 0.026$ and $Ra = 10^5$ whereas only single primary circulation cell in each half of the cavities occur for $Pr = 0.7, 1000$. The isotherms are highly compressed near the side walls especially for $\varphi = 45^\circ$ and 30° and the central regime at the top portion of the cavities are thermally well mixed. These observations are well explained with heatlines. The heatlines are highly dense at the central core of the cavity representing enhanced heat transport. The enhanced thermal mixing at the center is further attributed with the convective heat transport as seen from convective heatline cells. The large thermal gradient at the side walls is attributed by the heatfunctions with large variations. The heatlines near the edges of the bottom wall represent conductive heat transport for non-uniform heating of bottom wall. Overall heat transfer rates are found to be less for non-uniform heating case.

The heat transfer rates are further analyzed with local and average Nusselt numbers for the bottom and side walls. The non-uniform heating of bottom walls exhibit higher heat transfer rate at the central regime of the bottom wall. The local Nusselt numbers for the side wall illustrate that heat transfer rate is larger near the bottom portion. The local heat transfer rates at side walls are found to be larger for uniform heating situation (case 1). The variations of local Nusselt numbers are found to be correlated with heatfunctions. Average Nusselt numbers show that heat transfer rates are larger for uniform heating case. Average heat transfer rate is larger for $\varphi = 0^\circ$ with case 1 whereas the average heat transfer rates do not vary much with inclination angles with case 2. The heatline trajectories are found to be powerful to visualize the direction of heat flow for various shapes of containers and the application of heatlines concept in complex cavities has been evolved as a direct consequence of 'Bejan's heatline' concept.

Appendix A

The name "isoparametric" derives from the fact that the same parametric function describing the geometry may be used for interpolating spatial variable within an element. Fig. 2 shows a trapezoidal domain mapping to a square domain. The transformation between (x, y) and (ξ, η) coordinates can be defined by $X = \sum_{k=1}^{9} \Phi_k(\xi, \eta) x_k$ and $Y = \sum_{k=1}^{9} \Phi_k(\xi, \eta) y_k$ where (x_k, y_k) are the X, Y coordinates of the k nodal points as seen in Fig. 2a and b and $\Phi_k(\xi, \eta)$ is the basis function. The nine basis functions are:

$$\Phi_1 = (1 - 3\xi + 2\xi^2)(1 - 3\eta + 2\eta^2)$$

$$\Phi_2 = (1 - 3\xi + 2\xi^2)(4\eta - 4\eta^2)$$

$$\Phi_3 = (1 - 3\xi + 2\xi^2)(-\eta + 2\eta^2)$$

$$\Phi_4 = (4\xi - 4\xi^2)(1 - 3\eta + 2\eta^2)$$

$$\Phi_5 = (4\xi - 4\xi^2)(4\eta - 4\eta^2)$$

$$\Phi_6 = (4\xi - 4\xi^2)(-\eta + 2\eta^2)$$

$$\Phi_7 = (-\xi + 2\xi^2)(1 - 3\eta + 2\eta^2)$$

$$\Phi_8 = (-\xi + 2\xi^2)(4\eta - 4\eta^2)$$

$$\Phi_9 = (-\xi + 2\xi^2)(-\eta + 2\eta^2)$$

The above basis functions are used for mapping the trapezoidal domain into square domain and the evaluation of integrals of residuals (Eqs. (11)–(13), (16) and (19)).

References

[1] J.M. Garrpeters, The neutral stability of surface-tension driven cavity flows subject to buoyant forces 1. Transverse and longitudinal disturbances, Chem. Eng. Sci. 47 (5) (1992) 1247–1264.
[2] L.B. Wang, N.I. Wakayama, Control of natural convection in non- and low-conducting diamagnetic fluids in a cubical enclosure using inhomogeneous magnetic fields with different directions, Chem. Eng. Sci. 57 (11) (2002) 1867–1876.
[3] I.E. Sarris, I. Lekakis, N.S. Vlachos, Natural convection in a 2D enclosure with sinusoidal upper wall temperature, Num Heat Transfer A 42 (2002) 513–530.
[4] A. Ousegui, A. Le Bail, M. Havet, Numerical and experimental study of a natural convection thawing process, AIChE J. 52 (12) (2006) 4240–4247.
[5] O.G. Martynenko, P.P. Khramtsov, Free-Convective Heat Transfer, Springer, Berlin, 2005.
[6] J. Patterson, J. Imberger, Unsteady natural convection in a rectangular cavity, J. Fluid Mech. 100 (1980) 65–86.
[7] V.F. Nicolette, K.T. Yang, J.R. Lloyd, Transient cooling by natural convection in a two-dimensional square enclosure, Int. J. Heat Mass Transfer 28 (1985) 1721–1732.
[8] J.D. Hall, A. Bejan, J.B. Chaddock, Transient natural convection in a rectangular enclosure with one heated side wall, Int. J. Heat Fluid Flow 9 (1988) 396–404.
[9] J.M. Hyun, J.W. Lee, Numerical solutions of transient natural convection in a square cavity with different sidewall temperature, Int. J. Heat Fluid Flow 10 (1989) 146–151.
[10] T. Fusegi, J.M. Hyun, K. Kuwahara, Natural convection in a differentially heated square cavity with internal heat generation, Num. Heat Transfer A 21 (1992) 215–229.
[11] J.L. Lage, A. Bejan, The Ra–Pr domain of laminar natural convection in an enclosure heated from the side, Num. Heat Transfer A 19 (1991) 21–41.
[12] J.L. Lage, A. Bejan, The resonance of natural convection in an enclosure heated periodically from the side, Int. J. Heat Mass Transfer 36 (1993) 2027–2038.
[13] C. Xia, J.Y. Murthy, Buoyancy-driven flow transitions in deep cavities heated from below, ASME Trans. J. Heat Transfer 124 (2002) 650–659.
[14] A.M. Al-Amiri, K.M. Khanafer, Pop I, Numerical simulation of combined thermal and mass transport in a square lid-driven cavity, Int. J. Thermal Sci. 46 (7) (2007) 662–671.
[15] Y.E. Karyakin, Y.A. Sokovishin, O.G. Martynenko, Transient natural convection in triangular enclosures, Int. J. Heat Mass Transfer 31 (1988) 1759–1766.
[16] A. Bejan, D. Poulikakos, Natural convection in an attic shaped space filled with porous material, J. Heat Transfer – Trans. ASME 104 (1982) 241–247.
[17] D. Poulikakos, A. Bejan, Numerical study of transient high Rayleigh number convection in an attic-shaped porous layer, J. Heat Transfer – Trans. ASME 105 (1983) 476–484.
[18] L. Iyican, Y. Bayazitoglu, An analytical study of natural convective heat transfer within trapezoidal enclosure, ASME Trans. J. Heat Transfer 102 (1980) 640–647.
[19] Y.E. Karyakin, Transient natural convection in prismatic enclosures of arbitrary cross-section, Int. J. Heat Mass Transfer 32 (1989) 1095–1103.
[20] M. Perić, Natural convection in trapezoidal cavities, Num. Heat Transfer A 24 (1993) 213–219.
[21] R.A. Kuyper, C.J. Hoogendoorn, Laminar natural convection flow in trapezoidal enclosures, Num. Heat Transfer A 28 (1995) 55–67.
[22] M. Boussaid, A. Djerrada, M. Bouhadef, Thermosolutal transfer within trapezoidal cavity, Num. Heat Transfer A 43 (2003) 431–448.
[23] Y. Varol, H.F. Oztop, I. Pop, Numerical analysis of natural convection in an inclined trapezoidal enclosure filled with a porous medium, Int. J. Thermal Sci. 47 (10) (2008) 1316–1331.
[24] Y. Varol, H.F. Oztop, I. Pop, Natural convection in right-angle porous trapezoidal enclosure with partially cooled from inclined wall, Int. Commun. Heat Mass Transfer 36 (1) (2009) 6–15.
[25] S. Kimura, A. Bejan, The heatline visualization of convective heat-transfer, J. Heat Transfer – Trans. ASME 105 (4) (1983) 916–919.
[26] A. Bejan, Convection Heat Transfer, third ed., Wiley, New York, 2004.
[27] V.A.F. Costa, Unification of the streamline, heatline and massline methods for the visualization of two-dimensional transport phenomena, Int. J. Heat Mass Transfer 42 (1) (1999) 27–33.
[28] V.A.F. Costa, Heatline and massline visualization of laminar natural convection boundary layers near a vertical wall, Int. J. Heat Mass Transfer 43 (20) (2000) 3765–3774.
[29] V.A.F. Costa, Unified streamline, heatline and massline methods for the visualization of two-dimensional heat and mass transfer in anisotropic media, Int. J. Heat Mass Transfer 46 (8) (2003) 1309–1320.

[30] V.A.F. Costa, Bejan's heatlines and masslines for convection visualization and analysis, Appl. Mech. Rev. 59 (3) (2006) 126–145.
[31] D. Littlefield, P. Desai, Buoyant laminar convection in a vertical cylindrical annulus, J. Heat Transfer – Trans. ASME 108 (4) (1986) 814–821.
[32] C.J. Ho, Y.H. Lin, Thermal-convection heat-transfer of air water layers enclosed in horizontal annuli with mixed boundary-conditions, Warme und Stoffubertragung – Thermo Fluid Dyn. 24 (4) (1989) 211–224.
[33] C.J. Ho, M.S. Wu, J.B. Jou, Analysis of buoyancy-aided convection heat-transfer from a horizontal cylinder in a vertical duct at low Reynolds-number, Warme und Stoffubertragung – Thermo Fluid Dyn. 25 (6) (1990) 337–343.
[34] C.J. Ho, Y.H. Lin, Natural-convection of cold water in a vertical annulus with constant heat-flux on the inner wall, J. Heat Transfer – Trans. ASME 112 (1) (1990) 117–123.
[35] H. Chattopadhyay, S.K. Dash, Numerical visualization of convective heat-transfer from a sphere-with and without radial mass efflux, Int. J. Num. Meth. Heat Fluid Flow 5 (8) (1995) 705–716.
[36] F.L. Bello-Ochende, A heat function formulation for thermal convection in a square cavity, Int. Comm. Heat Mass Transfer 15 (1988) 193–202.
[37] S.K. Aggarwal, A. Manhapra, Use of heatlines for unsteady buoyancy-driven flow in a cylindrical enclosure, J. Heat Trans. – Trans. ASME 111 (1989) 576–578.
[38] Q.H. Deng, G.F. Tang, Numerical visualization of mass and heat transport for conjugate natural convection/heat conduction by streamline and heatline, Int. J. Heat Mass Transfer 45 (11) (2002) 2373–2385.
[39] Fu-Yun Zhao, Di Liu, Guang-Fa Tang, Application issues of the streamline, heatline and massline for conjugate heat and mass transfer, Int. J. Heat Mass Transfer 50 (2007) 320–334.
[40] A.M. Morega, Magnetic field influence on the convective heat transfer in the solidification processes, Part 2, Rev. Roum. Sci. Tech. – Electrotech. Energ. 33 (2) (1988) 155–156.
[41] A.M. Morega, The heat function approach to the thermomagnetic convection of electroconductive melts, Rev. Roum. Sci. Tech. – Electrotech. Energ. 33 (4) (1988) 359–368.
[42] K. Hooman, H. Gurgenci, Heatline visualization of natural convection in a porous cavity occupied by a fluid with temperature-dependent viscosity, J. Heat Transfer – Trans. ASME 130 (2008). Article Number: 012501.
[43] M. Mobedi, Conjugate natural convection in a square cavity with finite thickness horizontal walls, Int. Commun. Heat Mass Transfer 35 (4) (2008) 503–513.
[44] F.Y. Zhao, D. Liu, G.F. Tang, Natural convection in an enclosure with localized heating and salting from below, Int. J. Heat Mass Transfer 51 (11–12) (2008) 2889–2904.
[45] Y. Varol, H.F. Oztop, M. Mobedi, I. Pop, Visualization of natural convection heat transport using heatline method in porous non-isothermally heated triangular cavity, Int. J. Heat Mass Transfer 51 (21–22) (2008) 5040–5051.
[46] J.N. Reddy, An Introduction to the Finite Element Method, McGraw-Hill, New York, 1993.
[47] T. Basak, S. Roy, A.R. Balakrishnan, Effects of thermal boundary conditions on natural convection flows within a square cavity, Int. J. Heat Mass Transfer 49 (23–24) (2006) 4525–4535.
[48] S. Roy, T. Basak, Finite element analysis of natural convection flows in a square cavity with non-uniformly heated wall(s), Int. J. Eng. Sci. 43 (8–9) (2005) 668–680.
[49] G.K. Batchelor, An Introduction to Fluid Dynamics, Cambridge University Press, 1993.